

Energy & Environmental Science

Advancing high-temperature electrostatic energy storage via linker engineering of metal-organic frameworks in polymer nanocomposites

Journal:	Energy & Environmental Science
Manuscript ID	EE-ART-09-2024-004085.R1
Article Type:	Paper
Date Submitted by the Author:	
Complete List of Authors:	Xie, Zongliang; Lawrence Berkeley National Laboratory, Huang, Zhiyuan; Lawrence Berkeley National Laboratory Li, He; Pennsylvania State University University Park, Materials Science and Engineering; Lawrence Berkeley National Laboratory, Molecular Foundry Xu, Tianlei; Xi'an Jiaotong University Zhao, Haoyu; University of Southern Mississippi, School of Polymer Science and Engineering Wang, Yunfei; University of Southern Mississippi Xi, Pang; Xi'an Jiaotong University Cao, Zhiqiang; University of Southern Mississippi, Polymer Science and Engineering Altoe, Virginia; Lawrence Berkeley National Laboratory Klivansky, Liana; Lawrence Berkeley National Laboratory Wang, Zaiyu; Lawrence Berkeley National Laboratory Shelton, Steven; Lawrence Berkeley National Laboratory Lai, Shiqi; Lawrence Berkeley National Laboratory Liu, Peng; Xi'an Jiaotong University Zhu, Chenhui; Lawrence Berkeley National Laboratory, Advanced Light Sources Connolly, Michael; Lawrence Berkeley National Laboratory, Molecular Foundry Gu, Xiaodan; University of Southern Mississippi, School of Polymer Science and Engineering Peng, Zongren; Xi'an Jiaotong University Zhang, Jian; Lawrence Berkeley National Laboratory, Liu, Yi; Lawrence Berkeley National Laboratory, Liu, Yi; Lawrence Berkeley Laboratory, Molecular Foundry

SCHOLARONE™ Manuscripts

Broader Context

Polymer-based electrostatic energy storage capacitors are essential components for advanced electronics and renewable energy systems. With expanding applications in areas such as electric vehicles, oil exploration, and pulsed power systems, there arises a critical need for polymer-based dielectrics with reliable performance at temperatures reaching 200 °C. However, current commercial polymers are confronted with limitations in maintaining electrical insulating properties under such demanding temperatures. We address the critical challenge of improving the storage performance of heat-resistant polymer dielectrics by compositing polyethyleneimide (PEI) with Zr-based metal-organic framework (MOF) nanofillers. Through linker engineering, we create a series of isostructural UiO-66 MOF fillers that exhibit diverse capabilities in impeding charge migration and minimizing energy loss in PEI. This approach results in the development of a PEI/UiO-66-F4 composite, showcasing record-high energy storage performance and exceptional cyclic stability at 200 °C. Our findings also underscore an unprecedented correlation between the electronic structures of MOF fillers and the composites' improved electrical breakdown strength and energy storage properties. This interdisciplinary strategy offers a rational pathway to leverage the remarkable structural diversity of MOFs for tailoring polymer composite materials for high-temperature electrostatic energy storage applications.

PAPER

Received 00th January 20xx, Accepted 00th January 20xx

DOI: 10.1039/x0xx000000x

Advancing high-temperature electrostatic energy storage via linker engineering of metal—organic frameworks in polymer nanocomposites

Zongliang Xie, ‡abc Zhiyuan Huang, ‡b He Li, ‡ab Tianlei Xu, c Haoyu Zhao, d Yunfei Wang, de Xi Pang, c Zhiqiang Cao, d Virginia Altoé, b Liana M. Klivansky, b Zaiyu Wang, ef Steve W. Shelton, b Shiqi Lai, bg Peng Liu, c Chenhui Zhu, e Michael D. Connolly, b Corie Y. Ralston, b Xiaodan Gu, d Zongren Peng, Jian Zhang b and Yi Liu

High-performance, thermally resilient polymer dielectrics are essential for film capacitors used in advanced electronic devices and renewable energy systems, particularly at elevated temperatures where conventional polymers fail to perform. Compositing polymers with nanofillers is a well-established approach to enhancing energy storage performance, though there remains a strong need for fillers with broad structural tunability and a clear structure-property relationship to further improve performance at elevated temperatures. Herein, we unravel the untapped potential of UiO-66 metal—organic framework (MOF) derivatives as exceptional nanofillers for tuning the properties of the widely used polyetherimide (PEI). By systematically varying the linker structures, we create a series of isostructural MOF fillers that exhibit contrasting capabilities in regulating the charge transport and energy storage capacities of the resulting composite films. Notably, capacitors based on composite films using the electron-deficient UiO-66-F4 show remarkable long-term charge-discharge stability and achieve ultrahigh discharged energy densities of 9.87 J cm⁻³ at 150 °C and 9.21 J cm⁻³ at 200 °C, setting a new benchmark for high-temperature flexible polymer composites. Through comprehensive experimental and theoretical analyses, we establish an unprecedented correlation between the MOF fillers' electronic structures and the composites' improved electrical breakdown strength and energy storage properties. These findings offer a rational pathway to harness the exceptional structural diversity of MOFs for the development of composite materials suitable for high-temperature electrostatic energy storage.

Introduction

Polymer-based electrostatic energy storage capacitors are essential components for high-power electrical and electronic systems, owing to their ultra-fast charging-discharging rates, high power densities, remarkable voltage-endurance and facile processability.^{1–12} As their applications continue to expand across sectors including electric vehicles, oil exploration, and

pulsed power systems, there arises a critical need to enhance the thermal endurance of polymer dielectrics to ensure reliable performance at temperatures up to 150 °C^{13–21} and 200 °C.^{22–34} However, current commercial dielectric polymers, such as polyimide (PI), polyetherimide (PEI) and fluorene polyester (FPE), known for their high thermal endurance characterized by high glass transition temperatures (T_g), are confronted with limitations in maintaining electrical insulating properties under such demanding temperatures. Such deficiency is reflected by a pronounced increase in leakage current (J) due to electrical and thermal co-assisted electron emission from electrodes. Concurrent with the thermally degraded insulating properties, their energy storage properties, characterized by discharged energy density (U_d) and the charge-discharge efficiency (η), are reduced significantly.

To develop higher-performance polymeric materials for high-temperature electrostatic capacitors, a hybrid approach combining polymer matrices and inorganic nanofillers has been extensively explored^{17–27,35,36} to produce nanocomposites with tunable multi-physical properties and improved energy storage performance at elevated temperatures. Contingent on the relative alignment of electronic band structures of the polymer and filler components, this approach introduces filler–matrix interfaces that serve as either traps to hinder charge migration or barriers to

^{a.} Materials Sciences Division, Lawrence Berkeley National Laboratory, Berkeley, CA 94720, USA. E-mail: yliu@lbl.gov

^{b.} The Molecular Foundry, Lawrence Berkeley National Laboratory, Berkeley, CA 94720, USA. E-mail: jianzhang@lbl.gov

^c State Key Laboratory of Electrical Insulation and Power Equipment, Xi'an Jiaotong University, Xi'an, Shaanxi 710049, P. R. China.

^{d.} School of Polymer Science and Engineering, Center for Optoelectronic Materials and Devices, The University of Southern Mississippi, Hattiesburg, MS 39406, USA.

e. Advanced Light Source, Lawrence Berkeley National Laboratory, Berkeley, CA 94720, USA.

Department of Chemistry and the Hong Kong Branch of the Chinese National Engineering Research Center for Tissue Restoration and Reconstruction, The Hong Kong University of Science and Technology, Hong Kong 999077, P. R. China

⁹ Department of Chemistry, University of California, Berkeley, CA 94720, USA.

[†] Electronic Supplementary Information (ESI) available. See DOI: 10.1039/x0xx00000x

[‡] These authors contributed equally to this work.

Paper

impede charge injection and hinder the propagation of the breakdown paths. 37-40 These modulations have been demonstrated to increase voltage endurance and reduce energy loss, thereby enhancing the energy density and efficiency of the composite materials. Various inorganic nanofillers, including silsesquioxane,²⁶ boron nitride nanosheet (BNNS)²⁷ have been utilized accordingly (Table S1). However, a high volume content (~5–10 vol%) is usually required to induce a substantial effect, which incurs challenges for scaled-up film fabrication. While recent studies have shown that subnanomaterials, such as phosphotungstic acid subnanosheets, can effectively enhance electrostatic energy storage properties of PEI at high temperatures with very low filler loading, there remains a strong need to explore a broader class of fillers beyond these nanomaterials for reliable fabrication of robust and highperformance composite dielectric films.

Metal–organic frameworks (MOFs) represent a versatile class of crystalline porous materials formed by linking metal nodes and organic linkers. Rooted in the conceptual framework of "reticular chemistry",⁴⁵ MOFs have received widespread attention for their highly tunable structures, adaptable for potential applications in gas storage, separation, sensing, catalysis and electrochemical energy storage.^{46–53} In the realm of electrostatic energy storage, while MOFs are recognized as novel dielectric materials,⁵⁴ only very recently have they emerged as fillers for polymer composites with improved dielectric properties,^{55–58} showing certain advancements in high-temperature electrostatic energy storage properties though still lagging behind those obtained with state-of-the-art inorganic

nanofillers.²² Moreover, current studies on polymer/MOF composites overlook the most exciting aspect of MOFs, that is, their enormous structural diversity derived from the versatile choice of metal nodes and organic linkers, has not been explored. By leveraging the power of reticular chemistry and establishing a rational structure-property relationship, one may tap into an extensive resource of structures to identify optimal filler candidates for composite films used in electrostatic capacitors. This approach holds the promise of unlocking the full potential of MOFs in high-temperature electrostatic energy storage applications.

Herein, we present a tailored study investigating the impact of structural variations of MOF fillers on the interfacial properties in their composites with PEI, which ultimately leads to extraordinary electrostatic energy storage properties. Highquality nanocomposite films were fabricated from a mixture of PEI and a series of Zr(IV)-based MOFs containing linkers with varying electron affinities (Fig. 1). Detailed experimental and theoretical studies have unraveled the intricate impact of MOFs' electronic structure on the dielectric properties of the resultant polymer composites. By tuning the electron affinity of these MOFs, the embedded microscopic polymer–MOF interfaces become more efficient in impeding charge migration and minimizing energy loss, culminating in the discovery of a PEI/MOF composite with record-high energy storage performance and exceptional cyclic stability at 200 °C at a 1 wt% filler loading ratio. The scalability of this approach was demonstrated through the production of large-size nanocomposite films, based upon which reproducible arrays of film capacitors were fabricated and exhibited consistent and enduring high-temperature energy storage capabilities.

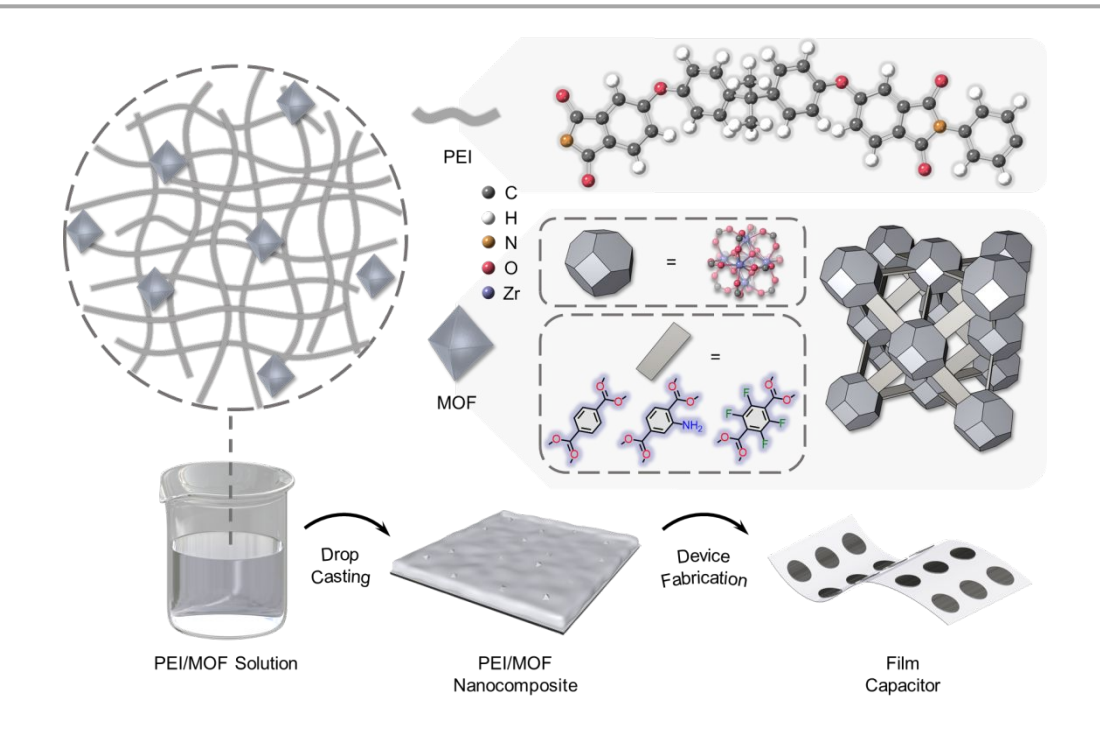


Fig. 1 Schematics illustrating the linker engineering of MOFs and the fabrication of PEI/MOF nanocomposite films. The octahedrons represent MOFs (UiO-66-H, UiO-66-NH₂ and UiO-66-F4), the polyhedrons represent metal clusters and the rectangles represent linkers.

Results and discussion, Experimental

MOF linker engineering for modulating interfacial charge transport

In composite materials, modulation of interfacial charge transport leverages the energy level mismatch between the filler components and the polymer matrix, which acts either as traps to capture charges or as barriers to impede charge injection and migration³⁷⁻⁴⁰. Since the effectiveness is contingent on the electronic band structures at the interfaces, the ability to tune the energy levels of the MOF fillers becomes essential for a systematic evaluation of the impact of band alignment on materials' endurance to strong electric fields. UiO-66, constructed from the 12-connected hexanuclear $[Zr_6O_4(OH)_4(O_2C-)_{12}]$ node and the ditopic 1 4benzodicarboxylic acid (BDC) linker, was chosen as an archetypal MOF for its robust synthesis, tunable structural diversity and high stability⁵⁹. Known as a relatively wide band gap material (~4.0 eV), the electronic structures of the parent UiO-66 can be readily tuned by using different linkers, allowing access to MOFs isostructural to UiO-66 with varying band gaps and energy levels. A series of MOFs was thus employed as the fillers to investigate their charge-trapping capabilities in polymer/MOF composites. Specifically, UiO-66-X (X = H, NH_2 , F4) correspond to MOFs incorporating ditopic BDC linkers with varying electronic affinities (Fig. 2a). The frontier orbital energy levels and the band gaps of these UiO-66 homologues were calculated using density functional theory (DFT) (primitive cells shown in Fig. S1, ESI†; DFT results shown in Fig. S2, ESI†) and plotted in Fig. 2a. UiO-66-F4 and UiO-66-NH2 have the lowest and highest conduction band (CB) energy levels amongst the series, respectively, in accordance with the electronic properties of the respective linkers due to the introduction of electronwithdrawing fluorides or the electron-donating amine groups. The relative band gap alignments are also consistent with the experimental results obtained from their optical spectra (Fig. S3). The electron affinity of PEI is similar²³ to that of the unsubstituted UiO-66-H, but higher than UiO-66-NH₂ and lower than UiO-66-F4. Such differences create a collection of interfaces with varying energy gaps, as defined by $\varphi = E_{\text{A-MOF}}$ – $E_{\text{A-PEI}}$. These gaps, presented as a barrier at the PEI–UiO-66-NH₂ interface and a trap at the PEI-UiO-66-F4 interface, are expected to more effectively restrict the migration of electrons and immobilize charges at high temperatures and electric fields than the PEI/UiO-66-H system. In addition, favourable interactions at PEI-MOF interfaces were supported by molecular dynamics simulation and DFT calculations. Such interactions were facilitated by hydrogen bonding interactions between the etheric oxygen atoms in PEI and the hydroxyl groups in the MOF clusters, and electrostatic interactions between the imide groups of PEI and the MOF clusters, as revealed by noncovalent interactions (NCI) analysis (Fig. 2b) and charge density differences between clusters of MOF and polymer chain segments Figs. S4 and S5).

Fabrication and characterization of polymer/MOF nanocomposites

The isostructural UiO-66-X series were synthesized following an acid-mediated hydrothermal approach (Table S2)⁵⁹⁻⁶¹, from which polycrystals with an average size of ~50 nm were obtained.

As confirmed by powder X-ray diffraction (PXRD) (Fig. S6), all of the MOF nanoparticles possessed the expected face-centered cubic (fcu) topology, consistent with the simulated patterns. The structures were featured by the distinctive peaks at 7.4° and 8.5°, representing the crystal planes (111) and (200), respectively. The relatively broader peaks of the as-synthesized MOFs are in accordance with the small particle sizes, as verified by scanning electron microscopy (SEM) and transmission electron microscopy (TEM) images (Fig. 2c and Figs. S7, S8). Analyses of their nitrogen sorption isotherms measured at 77 K revealed their permanent microporous nature (Fig. S9), with Brunauer-Emmett–Teller (BET) surface areas in the range of 708–1292 m² g⁻¹ (Table S3) and pore sizes less than 2 nm. The chemical compositions of MOF nanoparticles were corroborated by Fourier-transform infrared (FT-IR) spectroscopy (Fig. S10) and X-ray photoelectron spectroscopy (XPS) (Fig. S11).

Free-standing MOF-containing PEI nanocomposite films were prepared via a facile solution casting method (Fig. 1). Highquality large-area composite films (Fig. 2c) with 1.0 wt% loading of MOF nanoparticles were obtained with great uniformity (thickness ~12 µm), showing no observable filler particle aggregation throughout the polymer matrix (see SEM figures in Fig. 2c and Fig. S12). The results were further corroborated by atomic force microscopy-infrared spectroscopy (AFM-IR) measurements, supported by both wide-range IR scanning and IR mapping at characteristic wavenumbers (1404 cm⁻¹ for MOF and 1718 cm⁻¹ for PEI) (Fig. 2e and Figs. S13, S14). The results from Wide-Angle X-ray Scattering (WAXS) analysis indicate that all composites exhibit MOF crystallite peaks (Fig. 2f), confirming the well-maintained crystallinity of the MOF nanoparticles in the composite films. Differential scanning calorimetry (DSC) studies (Fig. S15) revealed no appreciable changes in T_g upon incorporation of the MOF fillers with PEI. Dynamic mechanical analysis (DMA) measurements indicated that the incorporation of MOF fillers resulted in improved Young's modulus from ~550 MPa for pure PEI to over 1000 MPa (Fig. S16). The considerable enhancement in mechanical modulus was attributed to favourable intermolecular interactions between MOF and PEI, as evidenced by NCI analysis⁶² (Fig. 2b and Figs. S4, S5). Small-angle X-ray scattering (SAXS) characterization was carried out to evaluate the mass fractal dimension ($D_{\rm m}$) of PEI/MOF composites, which was acquired from the ln[I(q)]-ln(q) plots (Fig. 2g) after fitting the equation $I(q) = q^{-\alpha}.55,56$ The higher $D_{\rm m}$ of PEI/MOF composites ($D_{\rm m} \sim 2.49 - 2.55$ nm) compared with PEI ($D_{\rm m} = 2.10$ nm) suggested relatively more compact microstructures and lower free volume in PEI/MOF composites than in PEI, resulting from good compatibility between MOF and polymer chains due to favourable interfacial interactions.

Dielectric characteristics and electrostatic energy storage performance

For electrostatic energy storage, it is critical to enhance both the dielectric constant (k) and the dielectric breakdown strength ($E_{\rm b}$) of polymers, given their crucial role in determining the maximum $U_{\rm d}$ in linear dielectric materials, as described by the equation:

$$U_{\rm d} = \eta \int \varepsilon_0 kE dE$$
 (Equation 1)

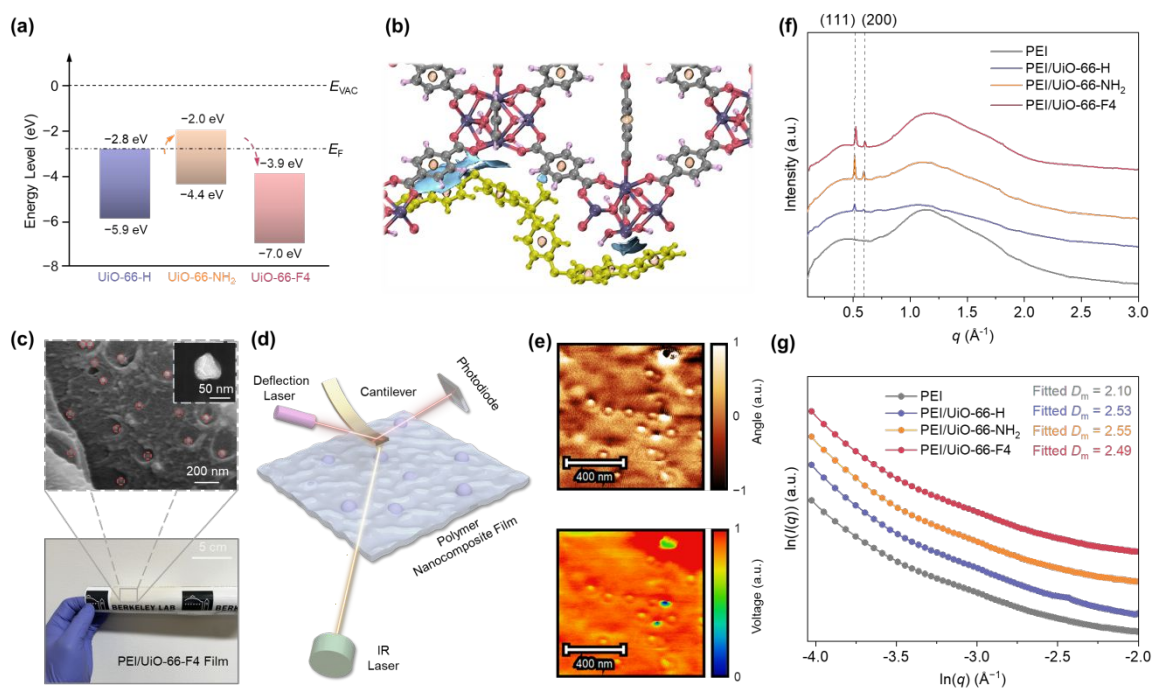


Fig. 2 (a) Calculated energy level diagrams of PEI and MOFs (UiO-66-H, UiO-66-NH $_2$ and UiO-66-F4), where EVAC represents the vacuum level and EF represents the Fermi level. (b) Illustration of simulated non-covalent interactions between a segment of PEI and MOF. PEI chain is highlighted in yellow. Gray-colored atoms represent C, pink-colored atoms represent H, red-colored atoms represent F, the blue-colored iso-surfaces indicate NCIs between PEI and MOF, the flesh-colored iso-surfaces indicate intramolecular interactions. (c) A large-area PEI/UiO66-F4 composite film at 1 wt% loading of MOF UiO66-F4, with a SEM image showing the well-dispersed MOF nanoparticles and a TEM image showing particle size ~50 nm). (d) Schematic diagram of AFM-IR measurement. (e) AFM phase image and AFM-IR mapping of the PEI/UiO66-F4 composite film probed at the wavenumber of 1718 cm $^{-1}$, confirming the dispersion of MOF particles within the PEI matrix. (f) WAXS curves of PEI and PEI/MOF composites. (g) SAXS curves of PEI and PEI/MOF composites plotted by double logarithmic curves, from which fractal dimension D_m were obtained from fitting.

where ε_0 represents the permittivity of free space, and E is the applied electric field. Dielectric spectroscopic studies revealed that the addition of MOF particles resulted in universally improved k. For instance, k was improved from 3.16 for PEI to 3.59 for the PEI/UiO-66-F4 composite measured at 200 °C and 1 kHz (Fig. 3a and Fig. S17). The larger k may be related to the dipolar interactions between the oxygen atoms of the polymers and the zirconium metal ions within the MOFs. PEI/MOF composites also displayed high dielectric stability at different temperatures and frequencies. The tan δ of PEI and all the composites remained essentially constant (<0.005) at elevated temperatures at 1 kHz, while the frequency-dependent dielectric spectra measured at 200 °C showed that both k and tan δ remained steady under different frequencies.

To assess the effectiveness of MOF-induced charge trapping in composite films, the dielectric breakdown strength of pure PEI and PEI/MOF composites was evaluated at different temperatures using a two-parameter Weibull statistics:

$$P(E) = 1 - \exp(-(E/E_b))^{\beta}$$
 (Equation 2)

where E_b is the Weibull breakdown strength at 63.2% of cumulative failure probability and β is the shape parameter that reflects data dispersion. At a filler ratio of 1 wt%, all PEI/MOF composites showed a marked enhancement in high-temperature dielectric breakdown strength, among which PEI/UiO-66-F4 exhibited the highest Weibull E_b of 720.3 MV m⁻¹ at 150 °C and 680.8 MV m⁻¹ at 200 °C, corresponding to 37% and 54% increase compared to pristine PEI (Fig. 3b and Figs. S18–S20).

PEI/UiO-66-F4 also exhibited a higher β of 27.0 compared with PEI (β = 9.0), indicating improved dielectric reliability under harsh conditions (Table S4).

Another compelling indication of suppressed charge transport in PEI/MOF composites was manifested by the significantly reduced leakage current density (J) than the pure PEI film at elevated electric fields under 200 °C (Fig. 3c). The PEI/UiO-66-F4 film showed the lowest J amongst all the PEI/MOF composites. For instance, at 200 °C and 300 MV m⁻¹ and at a filler ratio of 1 wt%, the electrical conductivity (γ) was $2.19 \times 10^{-12} \text{ S m}^{-1}$ for PEI/UiO-66-H and $1.70 \times 10^{-12} \text{ S m}^{-1}$ for PEI/UiO-66-F4, much lower than 1.53×10⁻¹⁰ S m⁻¹ for pure PEI (Fig. S21a). The nearly two orders of magnitude reduction of PEI's electrical conductivity upon loading of UiO-66-F4 is indicative of effective mitigation of charge transport, correlating well with its anticipated electron trapping capability endowed by interfacial energy gaps between PEI and respective MOF. Further analysis of the charge transport behavior by fitting the field-dependent current curves with different conduction equations suggested a prevalent Schottky emission pathway at the lower electric field region (Fig. 3c and Fig. S21b), while in the higher field region, the hopping conduction pathway predominates (Fig. 3c and Fig. S21c). By fitting the high electric field conduction behaviour with the following hopping conduction equation, the charge hopping distance (λ) between charge trapping sites can be quantitatively assessed for PEI and PEI/MOF composites:

Journal Name ARTICLE

$$J(E,T) = 2ne\lambda v * \exp(\frac{-E_a}{K_B T}) * \sinh(\frac{\lambda eE}{2K_B T})$$
 (Equation 3)

where *n* is the carrier concentration in C m⁻³, *e* is the charge of the carriers that equals to 1.6×10^{-19} C, λ is the hopping distance, ν is the attempt-to-escape frequency in Hz, E_a is the activation energy in eV, and K_B is the Boltzmann constant that equals to 1.38×10^{-23} m² kg s⁻² K⁻¹.

The hopping distance in PEI underwent a notable decrease compared with that of the PEI/MOF composites. Among these, PEI/UiO-66-F4 displayed the shortest hopping distance of 1.02 nm, in contrast to 1.92 nm for pure PEI, and 1.11 nm for the PEI/UiO-66-NH₂ composite (Fig. 3c and Fig. S21c). As the hopping distance indicates the average spacing between trap sites, the smaller values observed in PEI/MOFs reflect the larger density of trap sites, supporting their better charge suppression capabilities.

Correlated with restricted leakage current, energy loss is significantly reduced in the PEI/MOF composites, as revealed by the representative electric displacement–electric field (D–E) loops and discharged energy density ($U_{\rm d}$) measured at 150 °C and 200 °C, respectively (Figs. S22, S23). Slimmer D–E loops were obtained for PEI/MOF composites with respect to those of pristine PEI, implying suppressed electrical conduction and less energy loss. The PEI/UiO-66-F4 composite exhibited the slimmest charging–discharging curve, as exemplified by the one measured at 450 MV m $^{-1}$ and 200 °C (Fig. S24). Under such conditions, the charge–discharge efficiency (η) of pristine PEI dropped precipitously to 43.3%, in contrast to the minimal drop

to 96.0% for the PEI/UiO-66-F4 composite. Impressively, at a η of 90%, PEI/UiO-66-F4 sustained an electric field of 700 MV m⁻¹ at 150 °C and 600 MV m⁻¹ at 200 °C. In comparison, the pure PEI could only withstand an electric field of up to 300 MV m⁻¹ at 150 °C and 250 MV m⁻¹ at 200 °C at the same η (Fig. S25).

With the simultaneous enhancement of breakdown strength and k, as well as suppressed energy loss (i.e., improved η), the discharged energy density (U_d) of PEI/MOFs showed great improvement compared to pristine PEI (Fig. 3d and Fig. S26). PEI/UiO-66-F4 exhibited the highest U_d among all PEI/MOF composites at the optimal filler loading ratio of 1 wt% (Figs. S27, S28 and Table S5). At η of 91.0%, it displayed an $U_{\rm d}$ of 6.45 J cm⁻³ at 200 °C and 600 MV m⁻¹, far exceeding the performance of pristine PEI under the same temperature and discharge efficiency. A maximum U_d of 9.21 J cm⁻³ was realized at 200 °C and 800 MV m⁻¹, which is more than twice that of the pristine PEI (Fig. S29). Such performance is among the highest for hightemperature polymeric dielectric films (Fig. 3e and Tables S6, S7), including lab-synthesized polymers (PSBNP-co-PTNI, 28 o-POFNB,³⁴ PI-oxo-iso,²⁹ PI-spiro-2.5,³² SO-PI,⁶³ sc-PEENA,³⁰ p-POCINB,³³ PONB-2Me5Cl⁶⁴) and polymer composites (FPI-PWNS,²² PEI-O-AOC,18 PEI-TE,24 H-Al₂O₃/PEI,³¹ FPI/PCBM,²⁵ FPE/ITIC-Cl,⁶⁵ PI-3.0,²⁶). Compared to the most commonly used benchmark BOPP film, PEI/UiO-66-F4 film displays both a higher U_d and a larger power density under 200 MV m⁻¹ (0.75 J cm⁻³ and 228.06 MW L⁻¹ for PEI/UiO-66-F4 tested at 200 °C versus 0.40 J cm⁻³ and 109.19 MW L⁻¹ for BOPP tested at 105 °C) (Fig. 3f).

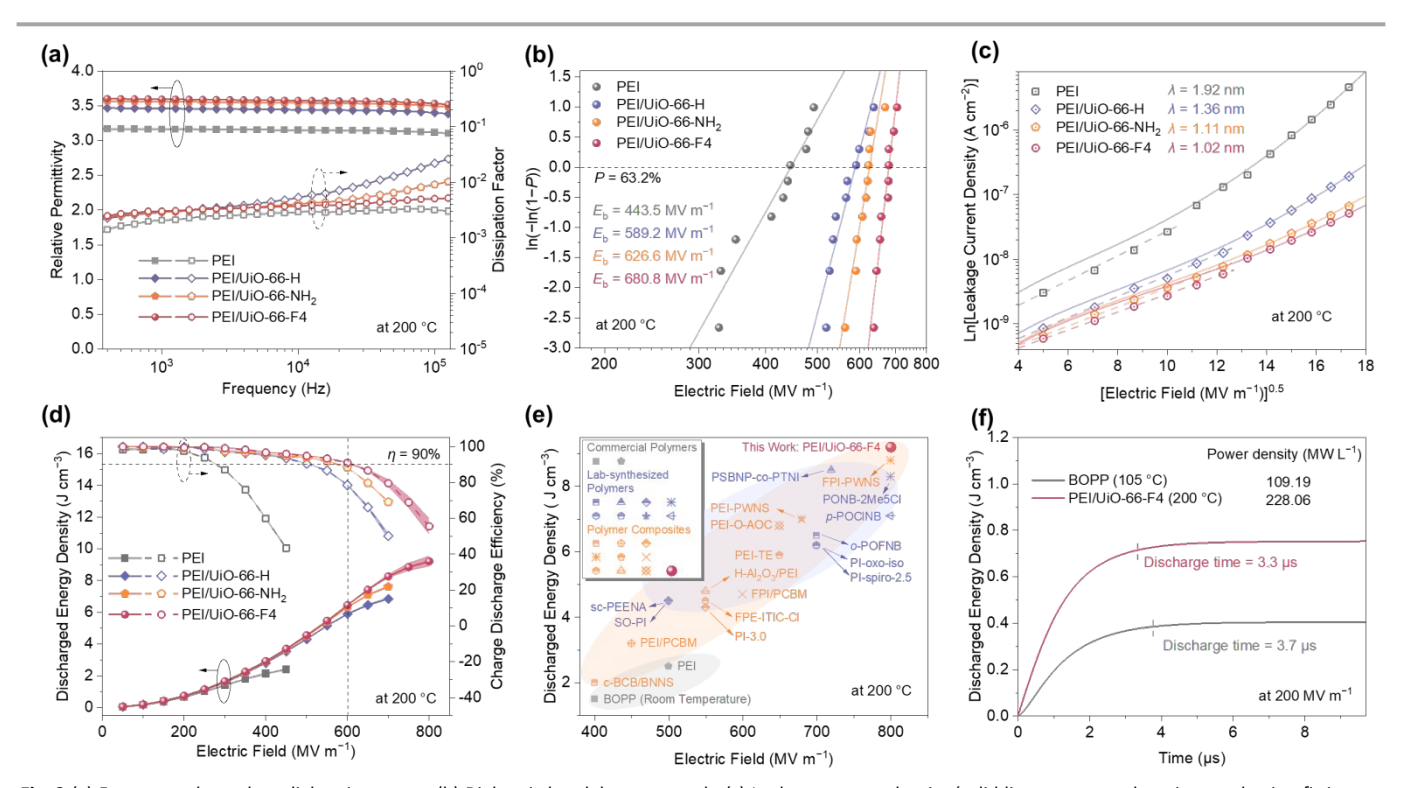


Fig. 3 (a) Frequency-dependent dielectric spectra, (b) Dielectric breakdown strength, (c) Leakage current density (solid lines represent hopping conduction fittings at higher electric field region and dotted lines represent linear fittings) and (d) Discharged energy density and charge—discharge efficiency of PEI and PEI/UiO-66-H, PEI/UiO-66-NH₂, PEI/UiO-66-F4 with 1 wt% filler loading at 200 °C. (e) Comparison of the maximum discharged energy density of PEI/UiO-66-F4 composites with 1 wt% filler loading against reported high-temperature polymer dielectrics at 200 °C. (f) Comparison of the power density of PEI/UiO-66-F4 (at 200 °C) and BOPP (at 105 °C).

Charge migration and trapping behaviours

The charge trapping mechanism can be further validated by stimulated depolarization current measurements. As indicated by the fitted curves of the TSDC results (Fig. 4a), in addition to the α relaxation peak⁶⁶ (Peak I, ~217 °C) observed in pure PEI, a new peak at ~230 °C (peak II) was observed in the cases of PEI/UiO-66-NH2 and PEI/UiO-66-F4 composite films. This new peak was attributed to the release of charges trapped at the PEI-MOF interfaces. In contrast, such feature was absent in the TSDC curve of the PEI/UiO-66-H composite (Fig. S30). Furthermore, the maximum depolarization current density determined from the TSDC curves of PEI/UiO-66-F4, which was positively related to the trap density, was approximately six times that observed for pure PEI. The observed deeper trap depth and higher trap density in PEI/UiO-66-F4 composite contribute to greater charge-capturing capability, subsequently leading to decreased leakage current under high temperature and high electric field conditions.

To further explore charge transport and charge trapping mechanism, as well as their effects on dielectric breakdown behaviors, we employed a numerical simulation, which is based on a modified two-dimensional bipolar charge transport-dielectric breakdown (2-D BCT-DB) model²⁰ (Fig. S31, Note S1 and Tables S8, S9). With an applied electric field of 500 MV m⁻¹ at 200 °C, both electrons and holes were injected from the respective electrodes, forming charge accumulation zones at the regions near the electrodes. A large amount of space charge

accumulation was observed in pristine PEI, with an integrated charge density of 11.72 C m⁻³, which caused severe electric field distortion at a degree of ~15% in the inner region of the film (Fig. 4b and Figs. S32, S33). In contrast, the injected charges could be effectively suppressed upon the addition of MOF nanoparticles, with UiO-66-F4 showing the best capability in restraining charge transport and alleviating charge accumulation (i.e., from 11.72 C m^{-3} of PEI to 7.34 C m^{-3} of PEI/UiO-66-F4). The formation of charge-accumulation zones near the electrode-polymer interface in PEI/UiO-66-F4 composite is beneficial for suppressing charge injection through the formation of a built-in electric field,²³ which further mitigates electric field distortion (~5% of electric field distortion for PEI/UiO-66-F4 versus ~15% for PEI, Fig. S33a). As a result, the large energy loss observed in PEI can be greatly restrained in PEI/UiO-66-F4, according to the simulated *D–E* loop results (Fig. S33b).

The electric field-concentrated region of polymer matrices with localized charge accumulation is typically the most vulnerable part that may initiate electrical breakdown. Due to the mitigated local electric field, as well as the mitigation of free charge transport with the addition of MOF nanoparticles, the electric tree propagation was restrained and the dielectric breakdown strength was therefore enhanced (Fig. 4b and Figs S34, S35). These simulations collectively provide a fundamental understanding of the origins of the improved dielectric performance and dynamic charge behaviours of the polymer/MOF composites.

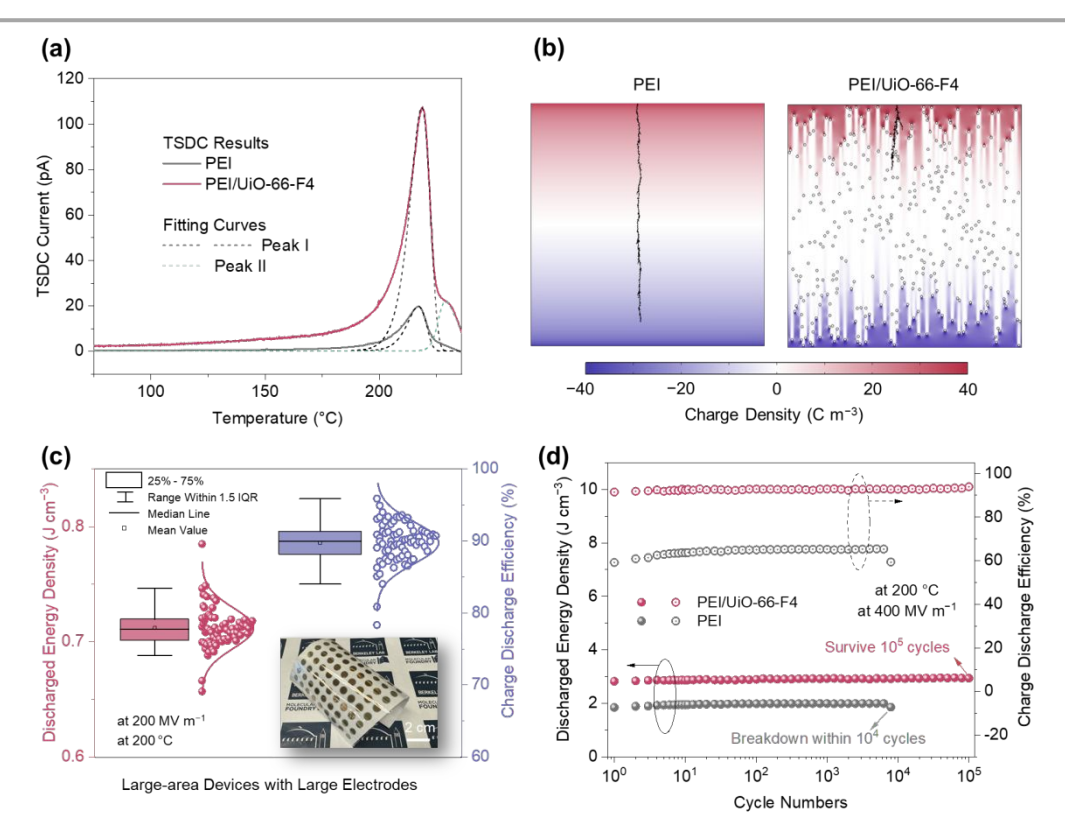


Fig. 4 (a) Comparison of thermally stimulated depolarization current (TSDC) curves of PEI and PEI/UiO-66-F4 composite. (b) Simulated charge distribution and electric tree propagation of PEI and PEI/UiO-66-F4 composite using a modified bipolar charge transport and dielectric breakdown (BCT-DB) model. (c) Interquartile range (IQR) analysis of energy storage characteristics of an array of 81 devices fabricated on a large-area PEI/UiO-66-F4 composite film with 1 wt% filler loading measured at 200 °C and 200 MV m⁻¹. The area of the film is 100 cm². (d) Cycling stability of devices based on PEI and the PEI/UiO-66-F4 composite with 1 wt% filler loading, measured at 200 °C and 400 MV m⁻¹.

Reliability and fatigue performance

To demonstrate the suitability of the PEI/UiO-66-F4 composite for scaling up, films with a large area of 15 cm × 10 cm were fabricated using the same drop-cast process. Devices fabricated at different regions of the same film showed negligible variations in $U_{\rm d}$ and η when tested under a harsh condition of 500 MV m⁻¹ and 200 °C (Fig. S36). An additional reliability test was conducted on an array of 81 devices fabricated evenly on the film with a larger electrode area at 200 MV m⁻¹ and 200 °C. The interquartile range (IOR) analysis reveals that the medium η is over 90% (Fig. 4c and Note S2), attesting to the high uniformity and stability of the composite film. Batch-to-batch experiments (Fig. S37) and fatigue testing (Fig. S38) further validated the consistency and high-temperature long-term operational stability of PEI/UiO-66-F4 composite films. Owing to its low energy loss and high dielectric breakdown strength, both U_d and η of the PEI/UiO-66-F4 film remained essentially unchanged after 10⁵ cycles at 400 MV m⁻¹ and 200 °C, while PEI only operated for less than 10⁴ cycles under the same condition with much lower $U_{\rm d}$ and η (Fig. 4d). In addition, a preliminary cost analysis showed that at a 1 wt% loading ratio, the cost of PEI/MOF composites increased only marginally (up to 10% for the most expensive variant, PEI/UiO-66-F4, see Table S10 and Fig. S39).

Conclusions

In this study, we rationalize the selection of MOF fillers for polymer composites for extreme-temperature electrostatic energy storage. The non-covalent interactions between MOF and PEI ensure good compatibility between components with the polymer nanocomposite, facilitating their processing into largescale, high-quality films. By varying the electron affinity of MOFs via linker engineering, the introduced polymer-MOF interfaces could serve as efficient trapping centers for capturing free charges and minimizing energy loss. The dependence of the dielectric properties of the resultant polymer composites on the electronic structures of the MOF fillers, as revealed by comprehensive experimental and theoretical studies, unveils the key factors relevant to the electrostatic energy storage performance at elevated temperatures. The linker engineering approach leads to an exceptional thermally resilient polymer composite film, which exhibits an ultrahigh U_d of 9.87 J cm⁻³ at 150 °C and 9.21 J cm⁻³ at 200 °C. At a discharge efficiency of 91% at 200 °C, a $U_{\rm d}$ of 6.45 J cm⁻³ is realized. Rigorous reliability assessments and fatigue tests underscore the superior quality and durability of the nanocomposite film devices, confirming their suitability for incorporation into energy storage systems that can endure thermal and electrical extremes. Through the identification of the optimal MOF filler via linker engineering, our results mark a significant advancement in discovering dielectric polymer composites with record performance for high-temperature electrostatic energy storage applications.

Experimental

Materials

Polyetherimide (PEI) pellets were purchased from PolyK Technologies. ZrCl₄, tetrahydrofuran (THF), *N*-methyl pyrrolidone (NMP), *N*, *N*-dimethylformamide (DMF), benzoic acid, formic acid, acetic acid (HAc), terephthalic acid, 2-aminoterephthalic acid and tetrafluoroterephthalic acid were purchased from Sigma-Aldrich. All reagents were used as received without further purification.

Synthesis of MOFs

In a typical process, the organic ligand (1 mmol) and ZrCl₄ (1 mmol) were suspended in the corresponding mixture of solvent and modulators (quantities listed in Table S2), and the reaction mixture was heated in an oven for 24 h to yield a powder product. The product was soaked in fresh solvent, DMF (3×10 mL) and methanol (3×10 mL), at room temperature (Table S2). Then the samples were centrifuged and dried under a vacuum at 120 °C overnight. The final product was kept in a vacuum dryer until used for further application.

Fabrication of polymer/MOF composites

MOF fillers were dispersed in NMP (1 mg mL⁻¹) via ultrasonication for 60 min. PEI pellets were magnetically stirred in NMP to yield a clear solution (40 mg mL⁻¹). For the fabrication of polymer/MOF composite films containing 0.2 wt%, 0.5 wt%, 1.0 wt%, and 2.0 wt% MOF, aliquots of MOF/NMP were added to the PEI/NMP solution at volumetric ratios of 1:12.5, 1:5, 1:2.5, and 1:1.25, respectively. The mixtures were then ultrasonicated for an additional 60 minutes. The resulting solution was immediately cast onto clean glass slides at room temperature and kept in an oven at 105 °C for 12 h. The thus-formed film was then peeled off in deionized water and annealed in a vacuum oven at 200 °C for 24 h. Pristine PEI film was fabricated by casting a PEI/NMP solution (40 mg mL⁻¹) under identical conditions.

Characterization

UV-vis absorption spectra of PEI and diffuse reflectance spectra of MOFs were obtained on an Agilent Cary 5000 UV-vis-NIR spectrometer. The optical transmittance of PEI and reflectance of MOFs were measured in the wavelength range 300-800 nm. Transmission electron microscopy (TEM) images of MOF nanoparticles were acquired at 200 kV using a JEOL 2100-F field emission scanning transmission electron microscope (STEM). Cross-sectional micromorphology characterizations of the nanocomposite films were conducted by FEI Nova NanoSEM 630. Powder X-ray diffraction (PXRD) patterns were recorded on a Rigaku X-ray diffractometer using Cu Kα radiation ($\lambda = 0.15418$ nm) at 40 kV and 20 mA. The infrared spectra were recorded in a Nicolet iS50 FTIR from ThermoFisher collected over the mid-IR region using a KBr beamsplitter and a built-in diamond crystal attenuated total reflectance (ATR). Nitrogen sorption measurements were conducted at 77 K on an ASAP 2020 sorption analyzer (Micromeritics Instrument Co., USA). The corresponding specific surface area was calculated by the Brunauer-Emmett-Teller (BET) method, and the pore size distributions were estimated from the adsorption isotherm by the quenched solid **Paper**

density functional theory (QSDFT) equilibrium model. Small/wide angle X-ray scattering (SAXS/WAXS) experiments were conducted on beamline 7.3.3 at Advanced Light Source in Berkeley Lawrence National Lab with an incident beam energy of 10 keV. Sample-to-detector distance (SDD) for SAXS and WAXS was around 3500 and 280 mm. The scattering signal was collected by a Pilatus 2M detector and processed using Igor 8 software combined with the Nika package. X-ray photoelectron spectroscopy (XPS) was performed in a Thermo Scientific™ K-AlphaPlusTM instrument equipped with monochromatic Al K α radiation (1486.7 eV) as the excitation source. The X-ray analysis area for measurement was set at 200×400 μm (ellipse shape) and a flood gun was used for charge compensation. The pass energy was 200 eV for the wide (survey) spectra and 50 eV for the high-resolution regions (narrow spectra). The base pressure of the analysis chamber was less than $\sim 1 \times 10^{-9}$ mbar. The analysis chamber pressure was at 1×10^{-7} mbar during data acquisition. A nanoIR3 AFM-IR from Anasys Instruments (Santa Barbara, CA) coupled to a MIRcat-QT quantum cascade, mid-infrared laser (frequency range of 917-1700 and 1900-2230 cm⁻¹ and repetition rate of 1470 kHz). AFM-IR data were collected in tapping mode using a gold-coated AFM probe (spring constant: 40 N m⁻¹ and resonant frequency [fo]: 300 kHz). The pulsed, mid-IR laser was tuned to resonance bands unique to each component as determined by FTIR characterization (1718 cm⁻¹ for PEI and 1404 cm⁻¹ for MOFs). Acquired images were flattened using Analysis Studio software.

Gold electrodes were sputtered on both sides of the polymeric films with a diameter of 6 mm for reliability and dielectric spectra testing. Frequency-dependent and temperaturedependent dielectric spectra over the frequency range between 100 Hz and 1 MHz and the temperature ranges from 20 °C to 200 °C of the samples were measured using an Agilent LCR meter (4294A), and a Delta Design 9023 oven was used to control the temperature. Gold electrodes were sputtered on both sides of the polymeric films with the size of 1 mm \times 1 mm for the following measurements. Electric displacement-electric field (D-E) loops were collected using a modified Sawyer-Tower circuit, where the samples were immersed in high-temperature insulating fluid and subjected to a triangular unipolar wave with a frequency of 100 Hz. Dielectric breakdown strengths were measured with a DC ramp voltage of 500 V s⁻¹ using a Trek 610E instrument as the voltage source. Leakage current densities were acquired by a Hewlett Packard 4140B pA meter using External Trek 1010BHS amplifier as a voltage source. Thermally stimulated depolarization current (TSDC) measurements were carried out in a Delta Design 9023 oven and the current was measured using a Hewlett Packard 4140B pA meter. The samples were firstly polarized under an electric field of 100 MV m⁻¹ at 220 °C for 10 min and then rapidly cooled down to 0 °C. The applied polarizing field was retained during the cooling process. The samples were kept at 0 °C for another 10 min with the polarizing field applied. After polarization, the samples were short-circuited and heated to 260 °C at a rate of 3 °C min⁻¹ during which the depolarization current was recorded.

DFT calculation

Molecular models construction

The molecular models of MOF and PEI were generated in the software package of Materials Studio (2019, Accelrys Software Inc.), in which the construction of MOF followed the Fm-3m (OH-5) symmetry group. To simplify the calculation scale, MOF was set as a primitive cell cleaved at the (110) crystal face, and PEI was set as a single chain with a polymerization degree of 1. After structural optimization through the Forcite module respectively, MOF and PEI were combined through layer settings and a vacuum slab was set up to avoid the impact of mirror molecules caused by periodic structures. The double-layer structure was then stabilized through dynamic and annealing simulation.

DFT calculation

First-principles density functional theory (DFT) simulation was performed in Castep software (Materials Studio 2019, Accelrys Software Inc.). OTFG ultra-soft pseudopotentials and generalized gradient approximation (GGA) with a Perdew–Burke–Ernzerhof (PBE) exchange correlation were used. The structure was optimized using a BFGS algorithm until the atomic forces converged to 0.05 eV Å⁻¹. In the DFT calculation, the differential charge density is defined as $\Delta \rho = \rho_{total} - \rho_1 - \rho_2$, where ρ_{total} is the total charge density of double-layered MOF-PEI structure, ρ_1 and ρ_2 represent the charge density of MOF layer and PEI layer, respectively.

CP2K calculation

The electronic calculation was carried out in the CP2K firstprinciples package, the input file of which was generated using the Multiwfn program ⁶⁷. The high symmetry path of MOF for band structure calculation was obtained by the Vaspkit program. Band gaps and molecular orbitals were calculated using a HLE17 exchange-correlation function. The geometry optimization of the double-layered MOF-PEI structure was conducted using a Perdew-Burke-Ernzerhof (PBE) exchange correlation functional and a 6-31G* basis set. A plane-wave basis was set with an energy cutoff of 400 eV and the optimization was completed after the SCF tolerance reached 3*10⁻⁶ eV atom⁻¹. Noncovalent interaction (NCI) analysis of the optimized model was performed using the Multiwfn program and the interaction force diagram was drawn in the VMD program.

Finite element modelling

A bipolar charge transport-dielectric breakdown (BCT-DB) model was used to simulate time-dependent charge behaviours, electric field distributions and dielectric breakdown propagation paths, by solving partial differential equations (current continuity equation, the Poisson equation and the transport equation) by using COMSOL Multiphysics version 6.0 with MUMPS and conjugate solver.

Author contributions

Y.L., H.L., Z.X. and Z.H. conceived the idea; Y.L., H.L., Z.X. and Z.H. designed the experiments; T.X. carried out DFT and MD

Journal Name ARTICLE

simulations with help from Z.X. under the supervision of Y.L., P.L. and Z.P.; X.P. carried out BCT-DB simulations with help from Z.X. under the supervision of Y.L., P.L. and Z.P.; Z.H. and S.L. conducted MOF synthesis and characterization under the supervision of M.C., C.R., Y.L. and J.Z.; Z.X. and H.L. prepared device samples for measurements under the supervision of Y.L.; Z.X., Z.H., V.A., L.M.K. and S.W.S. carried out structural, electrical, thermal and optical experiments under the supervision of Y.L.; H.Z. conducted AFM-IR tests under the supervision of X.G.; Z.C. conducted mechanical tests under the supervision of X.G.; Y.W. conducted SAXS and WAXS tests under the supervision of X.G. and C.Z.; Z.W. conducted WAXS test; Z.X., Z.H. and H.L. analysed the data; Y.L., Z.X., Z.H. and H.L. wrote the first version of the manuscript; All authors discussed the results and provided inputs to the manuscript.

Conflicts of interest

There are no conflicts to declare.

Acknowledgements

Z.X., H.L. and Y.L. acknowledge the support from the U.S. Department of Energy, Office of Science, Office of Basic Energy Sciences, Materials Sciences and Engineering Division, under Contract no. DE-AC02-05CH11231 within Inorganic/Organic Nanocomposites Program (KC3104). The synthesis and development of MOFs was supported by the Defense Threat Reduction Agency under award no. HDTRA241074. X.G. acknowledges the support from the U.S. Department of Energy, Office of Science, Office of Basic Energy Science under award no. DE-SC0022050. Work at the Molecular Foundry was supported by the Office of Science, Office of Basic Energy Sciences, of the U.S. Department of Energy under Contract no. DE-AC02-05CH11231. This research used beamline 7.3.3 of the Advanced Light Source, which is a DOE Office of Science User Facility under contract no. DE-AC02-05CH11231. Y.W. was supported in part by an ALS Doctoral Fellowship in Residence. The authors thank Dr. Antoine Lainé, Prof. Miquel Salmeron, Prof. Ting Xu, Dr. Eric Dailing, Dr. Zhen Xu, Dr. Qingsong Zhang and Dr. Lu Fan for discussions on experimental results, Haijuan Zhang and Dr. Shihai Zhang for instrumental and technical support.

Notes and references

- T.-Y. Wang, J. Mao, B. Zhang, G.-X. Zhang and Z.-M. Dang, Nat. Rev. Electr. Eng., 2024, 1, 516.
- 2 T. Zhang, H. Sun, C. Yin, Y. H. Jung, S. Min, Y. Zhang, C. Zhang, Q. Chen, K. J. Lee and Q. Chi, *Prog. Mater. Sci.*, 2023, 140, 101207.
- 3 J. Chen, Z. Pei, B. Chai, P. Jiang, L. Ma, L. Zhu, and X. Huang, Adv. Mater., 2023, 2308670, DOI: 10.1002/adma.202308670.
- 4 Q. Zhang, X. Chen, B. Zhang, T. Zhang, W. Lu, Z. Chen, Z. Liu, S. H. Kim, B. Donovan, R. J. Warzoha, E. D. Gomez, J. Bernholc and Q. M. Zhang, *Matter*, 2021, 4, 2448.
- 5 D. Q. Tan, Adv. Funct. Mater., 2020, 30, 1808567.
- M. Yang, M. Guo, E. Xu, W. Ren, D. Wang, S. Li, S. Zhang, C.-W. Nan and Y. Shen, *Nat. Nanotech.*, 2024, 19, 588.

- 7 Q.-K. Feng, S.-L. Zhong, J.-Y. Pei, Y. Zhao, D.-L. Zhang, D.-F. Liu, Y.-X. Zhang and Z.-M. Dang, *Chem. Rev.*, 2022, **122**, 3820.
- 8 J.-Y. Pei, L.-J. Yin, S.-L. Zhong and Z.-M. Dang, *Adv. Mater.*, 2023, **35**, 2203623.
- H. Li, Y. Zhou, Y. Liu, L. Li, Y. Liu and Q. Wang, Chem. Soc. Rev., 2021, 50, 6369.
- 10 X.-J. Liu, M.-S. Zheng, G. Chen, Z.-M. Dang and J.-W. Zha, *Energy Environ. Sci.*, 2022, **15**, 56.
- 11 C. Wu, A. A. Deshmukh, L. Chen, R. Ramprasad, G. A. Sotzing and Y. Cao, *Matter*, 2022, **5**, 2615.
- 12 Q. Li, F.Z. Yao, Y. Liu, G. Zhang, H. Wang and Q. Wang, Ann. Rev. Mater. Res., 2018, 48, 219.
- 13 H. Li, B. S. Chang, H. Kim, Z. Xie, A. Lainé, L. Ma, T. Xu, C. Yang, J. Kwon, S. W. Shelton, L. M., Kilvansky, V. Altoé, B. Gao, A. M. Schwartzberg, Z. Peng, R. O. Ritchie, T. Xu, M. Salmeron, R. Ruiz, K. B. Sharpless, P. Wu and Y. Liu, *Joule*, 2023, 7, 95.
- 14 Y. Wang, Z. Bao, S. Ding, J. Jia, Z. Dai, Y. Li, S. Shen, S. Chu, Y. Yin and X. Li, Adv. Mater., 2024, 36, 2308597.
- 15 Z. Pan, L. Li, L. Wang, G. Luo, X. Xu, F. Jin, J. Dong, Y. Niu, L. Sun, C. Guo, W. Zhang, Q. Wang and H. Wang, Adv. Mater., 2023, 35, 2207580.
- 16 C. Wu, A. A. Deshmukh, O. Yassin and Y. Cao, P. Nat. Acad. Sci., 2021, 118, e2115367118.
- 17 J. Chen, Z. Pei, Y. Liu, K. Shi, Y. Zhu, Z. Zhang, P. Jiang and X. Huang, *Adv. Mater.*, 2023, **35**, 2306562.
- 18 M. Yang, S. Wang, J. Fu, Y. Zhu, J. Liang, S. Cheng, S. Hu, J. Hu, J. He and Q. Li, *Adv. Mater.*, 2023, 35, 2301936.
- 19 Y. Cheng, Y. Feng, Z. Pan, P. Wang, J. Liu, L. Liang, J. Yu, J. Zhai and Q. Wang, *Energy Environ. Sci.*, 2023, **16**, 5881.
- 20 Z. Xie, K. Le, H. Li, X. Pang, T. Xu, V. Altoé, L. M. Klivansky, Y. Wang, Z. Huang, S. W. Shelton, X. Gu, P. Liu, Z. Peng and Y. Liu, Adv. Funct. Mater., 2024, 34, 2314910.
- 21 L. Ren, H. Li, Z. Xie, D. Ai, Y. Zhou, Y. Liu, S. Zhang, L. Yang, X. Zhao, Z. Peng, R. Liao and Q. Wang, *Adv. Energy Mater.*, 2021, 11, 2101297.
- 22 M. Yang, H. Li, J. Wang, W. Shi, Q. Zhang, H. Xing, W. Ren, B. Sun, M. Guo, E. Xu, N. Sun, L. Zhou, Y. Xiao, M. Zhang, Z. Li, J. Pan, J. Jiang, Z. Shen, X. Li, L. Gu, C.-W. Nan, X. Wang and Y. Shen, *Nat. Energy*, 2024, **9**, 143.
- 23 C. Yuan, Y. Zhou, J. Zhu, J. Liang, S. Wang, S. Peng, Y. Li, S. Cheng, M. Yang, J. Hu, B. Zhang, R. Zeng, J. He and Q. Li, *Nat. Commun.*, 2020, 11, 3919.
- 24 M. Yang, L. Zhou, X. Li, W. Ren and Y. Shen, Adv. Mater., 2023, 35, 2302392.
- 25 W. Ren, M. Yang, L. Zhou, Y. Fan, S. He, J. Pan, T. Tang, Y. Xiao, C.-W. Nan and Y. Shen, *Adv. Mater.*, 2022, 34, 2207421.
- 26 J. Dong, L. Li, P. Qiu, Y. Pan, Y. Niu, L. Sun, Z. Pan, Y. Liu, L. Tan, X. Xu, C. Xu, G. Luo, Q. Wang and H. Wang, Adv. Mater., 2023, 35, 2211487.
- 27 Q. Li, L. Chen, M. R. Gadinski, S. Zhang, G. Zhang, H. U. Li, E. Iagodkine, A. Haque, L.-Q. Chen, T. N. Jackson and Q. Wang, *Nature*, 2015, 523, 576.
- 28 J. Chen, Y. Zhou, X. Huang, C. Yu, D. Han, A. Wang, Y. Zhu, K. Shi, Q. Kang, P. Li, P. Jiang, X. Qian, H. Bao, S. Li, G. Wu, X. Zhu and Q. Wang, *Nature*, 2023, 615, 62.
- 29 R. Wang, Y. Zhu, J. Fu, M. Yang, Z. Ran, J. Li, J. Li, M. Li, J. Hu, J. He and Q. Li, *Nat. Commun.*, 2023, 14, 2406.
- 30 W. Xu, C. Zhou, W. Ji, Y. Zhang, Z. Jiang, F. Bertram, Y. Shang, H. Zhang and C. Shen, *Angew. Chem. Int. Ed.*, 2024, 63, e202319766.
- 31 M. Yang, Y. Zhao, Z. Wang, H. Yan, Z. Liu, Q. Li and Z.-M. Dang, *Energy Environ. Sci.*, 2024, **17**, 1592.
- 32 Z. Ran, R. Wang, J. Fu, M. Yang, M. Li, J. Hu, J. He and Q. Li, *Adv. Mater.*, 2023, **35**, 2303849.
- 33 S. Shukla, C. Wu, A. Mishra, J. Pan, A. P. Charnay, A. Khomane, A. Deshmukh, J. Zhou, M. Mukherjee, R. Gurnani,

Paper

- P. Rout, R. Casalini, R. Ramprasad, M. D. Fayer, P. Vashishta, Y. Cao and G. Sotzing, *Adv. Mater.*, 2024, **36**, 2402133.
- 34 A. Deshmukh, C. Wu, O. Yassin, A. Mishra, L. Chen, A. Alamri, Z. Li, J. Zhou, Z. Mutlu, M. Sotzing, P. Rajak, J. Vellek, M. A. Baferani, M. Cakmak, P. Vashishta, R. Ramprasad, Y. Cao and G. Sotzing, *Energy Environ. Sci.*, 2022, 15, 1307.
- 35 H. Li, E. Vargo, Z. Xie, L. Ma, P. F. Pieters, S. W. Shelton, A. P. Alivisatos, T. Xu and Y. Liu, *Adv. Mater.*, 2021, 36, 2401954.
- 36 B. V. Tawade, M. Singh, I. E. Apata, J. Veerasamy, N. Pradhan, A. Karim, J. F. Douglas and D. Raghavan, *J. Am. Chem. Soc. Au*, 2023, **3**, 1365.
- 37 Z. Meng, T. Zhang, C. Zhang, Y. Shang, Q. Lei and Q. Chi, Adv. Mater., 2023, 2310272. DOI: 10.1002/adma.202310272.
- 38 J.-W. Zha, M. Xiao, B. Wan, X. Wang, Z.-M. Dang and G. Chen, *Prog. Mater. Sci.*, 2023, **140**, 101208.
- 39 X. Wu, A. Karlin, V. Beilin, G. E. Shter, G. S. Grader, Y. Ivry,
 S. Lin and D. Q. Tan, *Adv. Mater.*, 2024, 36, 2401597.
 40 H. Luo, X. Zhou, C. Ellingford, Y. Zhang, S. Chen, K. Zhou,
- 40 H. Luo, X. Zhou, C. Ellingford, Y. Zhang, S. Chen, K. Zhou, D. Zhang, C. R. Bowen and C. Wan, *Chem. Soc. Rev.*, 2019, 48 4424
- 41 D. Ai, H. Li, Y. Zhou, L. Ren, Z. Han, B. Yao, W. Zhou, L. Zhao, J. Xu and Q. Wang, Adv. Energy Mater., 2020, 10, 1903881.
- 42 B. Sun, P. Hu, X. Ji, M. Fan, L. Zhou, M. Guo, S. He and Y. Shen, *Small*, 2022, **18**, 2202421.
- 43 Y. Zhou, C. Yuan, S. Wang, Y. Zhu, S. Cheng, X. Yang, Y. Yang, J. Hu, J. He and Q. Li, *Energy Storage Mater.*, 2020, 28, 255.
- 44 M. Yang, F. Yuan, W. Shi, W. Ren, M. Guo, C. Ouyang, L. Zhou, N. Sun, Y. Xiao, E. Xu, X. Zhang, Y. Wei, X. Deng, C. Nan, X. Wang and Y. Shen, Adv. Funct. Mater., 2023, 33, 2214100.
- 45 R. Freund, S. Canossa, S. M. Cohen, W. Yan, H. Deng, V. Guillerm, M. Eddaoudi, D. G. Madden, D. Fairen-Jimenez, H. Lyu, L. K. Macreadie, Z. Ji, Y. Zhang, B. Wang, F. Haase, C. Wöll, O. Zaremba, J. Andreo, S. Wuttke and C. S. Diercks, *Angew. Chem. Int. Ed.*, 2021, 60, 23946.
- 46 M. Eddaoudi, J. Kim, N. Rosi, D. Vodak, J. Wachter, M. O'Keeffe and O. M. Yaghi, *Science*, 2022, 295, 469.
- 47 H.-C. Zhou and S. Kitagawa, Chem. Soc. Rev., 2014, 43, 5415.
- 48 N. C. Burtch, J. Heinen, T. D. Bennett, D. Dubbeldam and M. D. Allendorf, *Adv. Mater.*, 2018, **30**, 1704124.
- 49 A. Dhakshinamoorthy, Z. Li and H. Garcia, *Chem. Soc. Rev.*, 2018, 47, 8134.
- 50 S. Zhou, O. Shekhah, A. Ramírez, P. Lyu, E. Abou-Hamad, J. Jia, J. Li, P. M. Bhatt, Z. Huang, H. Jiang, T. Jin, G. Maurin, J. Gascon and M. Eddaoudi, *Nature*, 2022, **606**, 706.
- 51 X. Shi, H. Li, T. Chen, Y. Duan, D. Shi, C. Kang, Z. Zhang and D. Zhao, *Nat. Chem. Eng.*, 2024, 1, 483.
- 52 C. Liu, Y. Bai, W. Li, F. Yang, G. Zhang and H. Pang, *Angew. Chem. Int. Ed.*, 2022, **61**, e202116282.
- 53 L. Su, S. Zhang, H. Wu, S. Zhou, C. Cui and H. Pang, *Nano Energy*, 2024, **130**, 110177.
- 54 A. I. Inamdar, S. Kamal., M. Usman, M.-H. Chiang and K.-L. Lu, *Coordin. Chem. Rev.*, 2024, **502**, 2115596.
- 55 X. Liu, D. Chen, J. Li, S.-L. Zhong, Y. Feng, D. Yue, D. Sheng, H. Chen, X. Hao and Z.-M. Dang, *Adv. Mater.*, 2024, 36, 2402220
- 56 J. Li, X. Liu, B. Huang, D. Chen, Z. Chen, Y. Li, Y. Feng, J. Yin, H. Yi and T. Li, *Mater. Horiz.*, 2023, **10**, 3651.
- 57 F. Wang, J. Cai, C. Yang, H. Luo, X. Li, H. Hou, G. Zou and D. Zhang, *Small*, 2023, **19**, 2300510.
- 58 Y. Li, J. Yin, Y. Feng, J. Li, H. Zhao, C. Zhu, D. Yue, Y. Liu, B. Su and X., Liu, *Chem. Eng. J.*, 2022, **429**, 132228.

- 59 J. H. Cavka, S. Jakobsen, U. Olsbye, N. Guillou, C. Lamberti, S. Bordiga and K. P. Lillerud, J. Am. Chem. Soc., 2008, 130, 13850.
- 60 Z. Hu, Y. Peng, Z. Kang, Y. Qian and D. Zhao, *Inorg. Chem.*, 2015, 54, 4862.
- 61 A. Schaate, P. Roy, A. Godt, J. Lippke, F. Waltz, M. Wiebcke and P. Behrens, *Chem. Eur. J.*, 2011, **17**, 6643.
- 62 T. Lu and Q. Chen, Comprehensive Comput. Chem., 2024, 2, 240
- 63 J. Dong, L. Li, Y. Niu, Z. Pan, Y. Pan, L. Sun, L. Tan, Y. Liu, X. Xu, X. Guo, Q. Wang & H. Wang, Adv. Energy Mater., 2024, 14, 2303732.
- 64 R. Gurnani, S. Shukla, D. Kamal, C. Wu, J. Hao, C. Kuenneth, P. Aklujkar, A. Khomane, R. Daniels, A. A. Deshmukh, Y. Cao, G. Sotzing and R. Ramprasad, *Nat. Commun.*, 2024, 15, 6107.
- 65 Y. Zhou, Y. Zhu, W. Xu and Q. Wang, Adv. Energy Mater., 2023, 13, 2203961.
- 66 M. Zhang, B. Zhu, X. Zhang, Z. Liu, X. Wei and Z. Zhang, Mater. Horiz., 2023, 10, 2455.
- 67 T. Lu and F. Chen, J. Comput. Chem., 2012, 33, 580.

Data Availability Statements (DAS)

The data supporting this article have been included as part of the Supplementary Information.